

ESAD: End-to-end Deep Semi-supervised Anomaly Detection

Chaoqin Huang
Shanghai Jiao Tong University
huangchaoqin@sjtu.edu.cn

Fei Ye
Shanghai Jiao Tong University
yf3310@sjtu.edu.cn

Ya Zhang
Shanghai Jiao Tong University
ya-zhang@sjtu.edu.cn

Yan-Feng Wang
Shanghai Jiao Tong University
wangyanfeng@sjtu.edu.cn

Qi Tian
Huawei Cloud & AI
tian.qil@huawei.com

Abstract

This paper explores semi-supervised anomaly detection, a more practical setting for anomaly detection where a small set of labeled outlier samples are provided in addition to a large amount of unlabeled data for training. Rethinking the optimization target of anomaly detection, we propose a new objective function that measures the KL-divergence between normal and anomalous data, and prove that two factors: the mutual information between the data and latent representations, and the entropy of latent representations, constitute an integral objective function for anomaly detection. To resolve the contradiction in simultaneously optimizing the two factors, we propose a novel encoder-decoder-encoder structure, with the first encoder focusing on optimizing the mutual information and the second encoder focusing on optimizing the entropy. The two encoders are enforced to share similar encoding with a consistent constraint on their latent representations. Extensive experiments have revealed that the proposed method significantly outperforms several state-of-the-arts on multiple benchmark datasets, including medical diagnosis and several classic anomaly detection benchmarks. Source code will be made publicly available.

1. Introduction

Anomaly detection, with broad application in medical diagnosis [47], credit card fraud detection [34], autonomous driving [16], and numerous other fields [6], has received significant attention among the machine learning community. For example, anomaly detection can quickly filter out the majority of disease-free patches in a given pathological slice, so that physicians can focus more on the disease-related area and save diagnosis time. The main challenge in anomaly detection is that anomalous samples are diverse and inexhaustible. To bypass the unfeasible task of collect-

ing a representative set of anomalous samples, many approaches [40, 33, 55] resort to unsupervised learning so that only normal samples are needed for model training.

A more practical setting of anomaly detection is semi-supervised anomaly detection, where a small set of labeled outlier samples are provided in addition to a large amount of unlabeled data for training. In the real-world scenario, it is easy to obtain a small fraction of ‘biased’ anomalous data (named labeled outliers). However, with the ‘bias’ in labeled outliers, earlier semi-supervised anomaly detection methods still follow the unsupervised learning paradigm [28, 19], and the labeled outliers are leveraged as certain forms of regularization. S²OC-SVM [28] extends the one-class SVM kernel by modeling the data marginal distribution with the graph Laplacian built from both labeled and unlabeled samples. [19] generalizes the Support Vector Data Description (SVDD) [45], a one-class classifier, to semi-supervised learning, where labeled outliers are required to lie outside the hypersphere. More recently, Deep SAD [39] is introduced as the first deep semi-supervised anomaly detection method. It builds upon *Infomax principle*, the unsupervised learning paradigm that maximizes the mutual information between the normal data and the latent representations and enforces an additional regularization on the latent representations, and incorporates the labeled data with the assumption that the entropy for normal data is lower than that of the labeled outliers. In its implementation, the maximization of mutual information and regularization cannot be achieved by end-to-end training. The two-stage process, as illustrated in Figure 1 (a), cannot guarantee the two losses are simultaneously optimized.

In this paper, rethinking the optimization target of anomaly detection, we start from a new objective function that measures the KL-divergence between normal and anomalous data. We prove that it can be transformed into two factors: (i) *mutual information* between the data and the latent representations, which guarantees the network learns

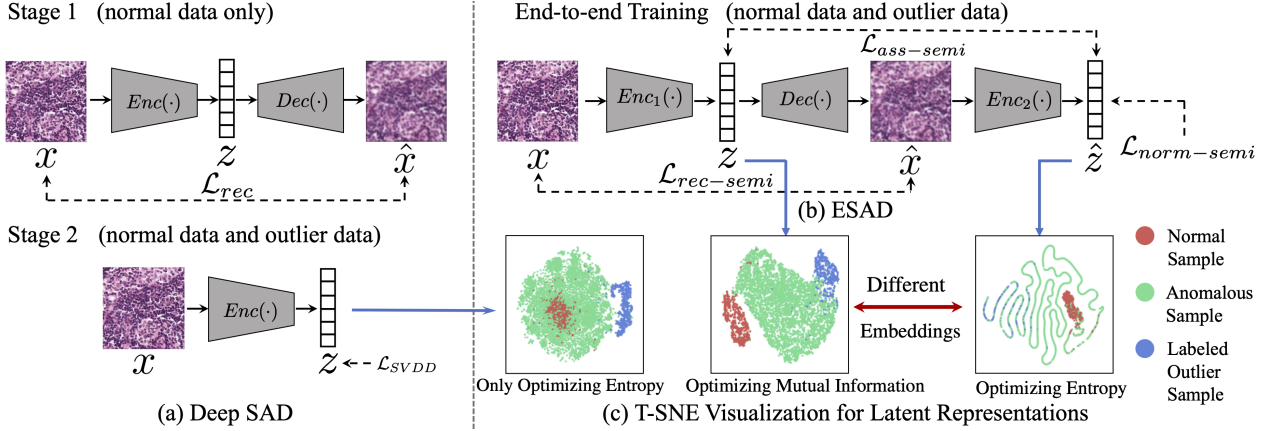


Figure 1. The training processes of (a) Deep SAD and (b) ESAD for semi-supervised anomaly detection. Deep SAD adopts a two-stage learning process. ESAD leverages an encoder-decoder-encoder structure, where the two encoders are enforced to share similar encoding with a consistent constraint on their latent representations, with the first encoder targeting to optimize the mutual information and the second encoder focusing on the entropy. (c) shows the T-SNE [25] visualization results for the latent representations. ESAD shows more distinctive features than Deep SAD. z and \hat{z} in ESAD shows different embeddings since they are targeting different optimizations.

good representations only for the normal data but not for the labeled outliers, and (ii) *entropy* of latent representations, which enforces the compacted representations (low entropy) for the normal data and scattered representations (high entropy) for the outliers. We show that these two factors are integral parts of the single objective function and hence need to be optimized simultaneously and be considered in the anomaly score measurement during the test. Different from Deep SAD [39], which abandons the optimization of the mutual information at the second training stage and only considers the entropy term during the test, we optimize these two factors simultaneously and incorporate them into both the training and testing phases.

There is a contradiction between the optimization of mutual information and entropy. For example, when the entropy of the latent representations is minimized to zero in the extreme case, the model can be considered as mapping all data into a constant in which the mutual information is also restricted to zero. It remains a great challenge to directly optimize the objective function within a single encoder due to the above contradiction. We thus propose a novel encoder-decoder-encoder structure, where two separate but closely resembled encoders are employed for emphasizing different aspects of the optimization and can be trained in an end-to-end fashion, naming as end-to-end semi-supervised anomaly detection (ESAD). The corresponding architecture is shown in Figure 1 (b). Specifically, the first encoder focuses on optimizing the mutual information and the second encoder focuses on optimizing the entropy, resulting in different embeddings (see Figure 1 (c)). Then the two encoders are enforced to share similar encoding with a consistent constraint on their latent representations. With this encoder-decoder-encoder structure,

ESAD manages to simultaneously optimize mutual information and entropy in an end-to-end fashion.

To validate the effectiveness of ESAD, we conduct experiments with medical images, including metastases detection in digital pathology [4] and disease recognition on chest X-Rays [49]. Besides medical images, we also conduct extensive experiments on three natural image benchmarks [23, 51, 22] and several classic anomaly detection benchmarks [37]. Results show that ESAD outperforms state-of-the-art methods on both medical image datasets and the classic benchmark datasets.

2. Related Works

Unsupervised Anomaly Detection. The vital challenge of unsupervised anomaly detection is that the training dataset contains only normal data. One-class classification based approaches tended to depict normal data with statistical approaches [15, 43, 52, 35, 38]. Self-supervised based approaches remedied the lack of supervision by introducing different self-supervisions, where the model was trained to optimize a self-supervised task, and then normal data can be separated with the assumption that anomalous data will perform differently. In this domain, reconstruction [41, 3, 50, 29, 42, 57, 12, 18] is the most popular self-supervision. [40] and [1] employed adversarial training to optimize the autoencoder and leveraged its discriminator to further enlarge the reconstruction error gap between normal and anomalous data. Other approaches tackled this problem by introducing other self-supervisions, e.g., [17] applied dozens of image geometric transforms and created a self-labeled dataset for transformation classification, and [53] proposed a restoration framework to further improve the feature learning.

Semi-supervised Anomaly Detection. Since classical

semi-supervised approaches [20, 36, 30, 10, 31], originating from a supervised classifier and based on the cluster assumption [7], are inappropriate and hardly detect new and unknown anomalies, the semi-supervised anomaly detection needs to ground on the unsupervised learning paradigm [19]. Along this line, Deep SSAD [19] has been studied recently in specific contexts such as videos [21], network intrusion detection [27], or specific neural network architectures [14]. Deep SAD [39], a general method based on deep SVDD [38], learned a neural-network mapping of the input that minimized the volume of data around a pre-determined point. The training of Deep SAD consists of two stages. In this paper, we propose an end-to-end training method for semi-supervised anomaly detection.

Anomaly Detection on Medical Images is an important application but rarely considered in deep anomaly detection literature. [56] proposed P-Net for anomaly detection in retinal images by leveraging the specific relation between the image texture and the regular structure of retinal images, which is hard to generalize to other medical data. [47] relied on the classical autoencoder approach with a re-designed training pipeline to handle high-resolution, complex images. [54] proposed a confidence-aware anomaly detection model, which consists of a shared feature extractor, an anomaly detection module, and a confidence prediction module for detecting viral pneumonia with in-house data. In this paper, we conduct experiments on some well-organized and open-source medical image datasets [4, 49].

3. End-to-end Deep Semi-supervised Anomaly Detection

In this section, we propose an *end-to-end semi-supervised anomaly detection method (ESAD)*. We propose a new KL-divergence based objective function, showing that the two factors: the mutual information between the data and the latent representations, and the entropy of latent representations, are indeed inseparable. To simultaneously optimize the two terms, we propose a novel model architecture to achieve end-to-end training. An anomaly score that considers both the mutual information and the entropy is used during the test phase.

3.1. Problem Formulation

Let \mathcal{X} and \mathcal{Z} be the domain of original data and latent representations. Denote \mathcal{X}_n be the set of normal data and \mathcal{X}_a be the set of anomalous data, where $\mathcal{X}_n = \{\mathbf{x}_n : \mathbf{x}_n \sim p_n(\mathbf{x})\}$, $\mathcal{X}_a = \{\mathbf{x}_a : \mathbf{x}_a \sim p_a(\mathbf{x})\}$. Let the corresponding representation of \mathcal{X}_n and \mathcal{X}_a to be \mathcal{Z}_n and \mathcal{Z}_a accordingly, where $p_n(\mathbf{z})$ and $p_a(\mathbf{z})$ are the marginal distribution of the latent representations, $p_n(\mathbf{x}, \mathbf{z})$ and $p_a(\mathbf{x}, \mathbf{z})$ are the joint distribution between the original data and the latent representations.

For anomaly detection, our goal is to distinguish the normal data \mathbf{x}_n and anomaly data \mathbf{x}_a . A common choice is to define a continuous and (almost everywhere) differentiable parametric function, $E_\theta : \mathcal{X} \rightarrow \mathcal{Z}$ with parameters θ (a neural network) that encodes the data to the low-dimensional representations and detect the anomaly data in the space \mathcal{Z} . To completely maximize the distance between normal and anomalous data in terms of the joint distribution for original data and latent representation, in which the distribution distance in image space is taken into consideration simultaneously, we take the commonly used KL divergence as the measurement metric, and the objective function can be formulated as:

$$\max_{\theta} \text{KL} [p_n(\mathbf{x}, \mathbf{z}) \parallel p_a(\mathbf{x}, \mathbf{z})]. \quad (1)$$

Note that when maximizing Eq. (1), all marginal distributions and all conditional distributions also match this maximization (see the supplementary material for the proof).

3.2. Optimization in the Semi-supervised Setting

In the training process of the semi-supervised anomaly detection, we are given N samples from $p_n(\mathbf{x})$, which we denote \mathcal{X}_n . In addition, we are given M labeled anomalous samples as outlier samples, denoted by \mathcal{X}_o , and we assume that $M \ll N$. Note that \mathcal{X}_o is very limited and cannot represent the range of possible anomalous data. Thus, it remains a great challenge to estimate $p_a(\mathbf{x}, \mathbf{z})$.

To tackle this problem, firstly, we decompose Eq. (1) into four components and investigate to bypass the components related to anomalous data. Let $I_n(\mathbf{x}, \mathbf{z})$ denotes the mutual information between \mathbf{x} and \mathbf{z} for normal data; $H_n(\mathbf{z})$ denotes the entropy of \mathbf{z} for normal data; $H(p_o(\mathbf{z}|\mathbf{x}), p_a(\mathbf{z}|\mathbf{x}))$ denotes the cross-entropy between $p_n(\mathbf{z}|\mathbf{x})$ and $p_a(\mathbf{z}|\mathbf{x})$; $\text{KL} [p_n(\mathbf{x}) \parallel p_a(\mathbf{x})]$ denotes the KL divergence between $p_n(\mathbf{x})$ and $p_a(\mathbf{x})$. Then Eq. (1) can be reformulated as:

$$\begin{aligned} & \max_{\theta} \text{KL} [p_n(\mathbf{x}, \mathbf{z}) \parallel p_a(\mathbf{x}, \mathbf{z})] \\ &= \max_{\theta} \{I_n(\mathbf{x}, \mathbf{z}) - H_n(\mathbf{z}) + \mathbb{E}_{p_n(\mathbf{x})} [H(p_n(\mathbf{z}|\mathbf{x}), p_a(\mathbf{z}|\mathbf{x}))] \\ & \quad + \text{KL} [p_n(\mathbf{x}) \parallel p_a(\mathbf{x})]\}. \end{aligned} \quad (2)$$

Eq. (2) is an equivalent reformulation (see the proof in the supplementary material). As the first and second components can be trained through an unsupervised fashion, the demand for anomalous data is reduced. For the third term, with the assumption that $p_n(\mathbf{x}, \mathbf{z})$ and $p_a(\mathbf{x}, \mathbf{z})$ have a certain distance, for most $\mathbf{x}, \mathbf{z} \sim p_n(\mathbf{x}, \mathbf{z})$, the evaluated density $p_a(\mathbf{z}|\mathbf{x})$ is small enough. Then we have $p_a(\mathbf{z}|\mathbf{x}) \leq p_n(\mathbf{z})$ and thus $p_a(\mathbf{z}|\mathbf{x}) \leq 1$. Then the non-negativity of

$\mathbb{E}_{p_n(\mathbf{x})} [H(p_n(\mathbf{z}|\mathbf{x}), p_a(\mathbf{z}|\mathbf{x}))]$ can be ensured:

$$\begin{aligned} & \inf \mathbb{E}_{p_n(\mathbf{x})} [H(p_n(\mathbf{z}|\mathbf{x}), p_a(\mathbf{z}|\mathbf{x}))] \\ &= \inf \mathbb{E}_{p_n(\mathbf{x}, \mathbf{z})} [-\log p_a(\mathbf{z}|\mathbf{x})] \\ &\geq \mathbb{E}_{p_n(\mathbf{x}, \mathbf{z})} [\inf (-\log p_a(\mathbf{z}|\mathbf{x}))] \\ &\geq 0. \end{aligned} \quad (3)$$

Moreover, the fourth term in Eq. (2) is a constant greater than zero since $p_n(\mathbf{x})$ and $p_a(\mathbf{x})$ are fixed. Then we have

$$\text{KL}[p_n(\mathbf{x}, \mathbf{z}) \| p_a(\mathbf{x}, \mathbf{z})] \geq I_n(\mathbf{x}, \mathbf{z}) - H_n(\mathbf{z}). \quad (4)$$

Thus, a lower bound to the KL in Eq. (2) is:

$$\max_{\theta} I_n(\mathbf{x}, \mathbf{z}) - H_n(\mathbf{z}). \quad (5)$$

Note that in Eq. (5), all the terms refer only to normal data. It gives an optimization method for the normal data, without dependence on the anomalous data. To be emphasized, the two factors in Eq. (5) are indeed inseparable. Considering only one of them cannot guarantee that the KL divergence in Eq. (1) is maximized.

For the small set of labeled outlier samples, different from the above optimization for the normal data, we resort to minimizing the KL divergence between the labeled outlier data and the real anomalous data, i.e., $\min_{\theta} \text{KL}[p_o(\mathbf{x}, \mathbf{z}) \| p_a(\mathbf{x}, \mathbf{z})]$, so that their latent representations are similar. Optimizing together with the normal data (Eq. (5)), the final objective function is:

$$\max_{\theta} \{[I_n(\mathbf{x}, \mathbf{z}) - I_o(\mathbf{x}, \mathbf{z})] - [H_n(\mathbf{z}) - H_o(\mathbf{z})]\}, \quad (6)$$

where $I_o(\mathbf{x}, \mathbf{z})$ denotes the mutual information between \mathbf{x} and \mathbf{z} for the labeled outlier data, and $H_o(\mathbf{z})$ denotes the entropy of \mathbf{z} for the labeled outlier data. The mutual information loss guarantees the network learns a good representation only for the normal data but not for the labeled outliers, while the entropy loss enforces the compacted representation (low entropy) for the normal data and scattered representation (high entropy) for the labeled outliers.

3.3. Model Architecture and Training Loss

We design the model architecture and the training loss for the optimization of the mutual information and the entropy as discussed in Section 3.2. Firstly, for the term of mutual information, we reformulate it as

$$\begin{aligned} & I(\mathbf{x}, \mathbf{z}) \\ &= H(\mathbf{x}) - H(\mathbf{x}|\mathbf{z}) \\ &= H(\mathbf{x}) + \mathbb{E}_{\mathbf{x} \sim p(\mathbf{x})} \mathbb{E}_{\mathbf{z} \sim p(\mathbf{z}|\mathbf{x})} [\log p(\mathbf{x}|\mathbf{z})], \end{aligned} \quad (7)$$

where the first term is a constant, the second term is the reconstruction likelihood. This indicates that the optimization of mutual information can be achieved in the form of

reconstruction. In the implementation, an autoencoder architecture takes \mathbf{x} as input, and attempts to reconstruct the original data:

$$\hat{\mathbf{x}} = \text{Dec}(\text{Enc}_1(\mathbf{x})), \quad (8)$$

where $\text{Enc}_1(\cdot)$ and $\text{Dec}(\cdot)$ indicate the encoder and decoder of the autoencoder, $\hat{\mathbf{x}}$ indicates the output of the autoencoder. For optimizing $I_n(\mathbf{x}, \mathbf{z})$ for the normal data and optimizing $-I_o(\mathbf{x}, \mathbf{z})$ for the labeled outlier data, a reconstruction loss is used for the training:

$$\mathcal{L}_{\text{rec-semi}} = \frac{1}{N} \sum_{i=1}^N \|\hat{\mathbf{x}}_i - \mathbf{x}_i\|^2 + \frac{1}{M} \sum_{j=1}^M \|\hat{\mathbf{x}}_j - \tilde{\mathbf{x}}_j\|^2, \quad (9)$$

where $\tilde{\mathbf{x}}$ is a transformed version of \mathbf{x} , i.e., $\tilde{\mathbf{x}} \neq \mathbf{x}$ (details are in the next paragraph). This learning strategy makes the autoencoder well reconstruct the normal data but erroneously reconstruct the labeled outlier samples. Note that the mutual information between the outlier samples and the latent representations is minimized, since the likelihood item, $\log p(\mathbf{x}|\mathbf{z})$, will be small when the autoencoder cannot well reconstruct the original data. *Thus, we provide a solid mathematical support for reconstruction-based anomaly detection methods and make a semi-supervised extension on the view of optimizing mutual information.*

To find the suitable version of $\tilde{\mathbf{x}}$, a feasible strategy is forcing the model to reconstruct the labeled outlier data to the normal data [33]. But this task is too strict and difficult, especially for two types of samples that are quite different, making the model hard to converge. We here propose a feasible strategy: for the data which is functioned as a vector, $\tilde{\mathbf{x}}$ can be a version adding Gaussian noise or a random permutation between various dimensions; for the image data, it can be a noised and rotated version of the original images. This greatly reduces the difficulty of the training and makes the usage of labeled outlier samples more efficient.

For the entropy $H(\mathbf{z})$, in this part, we target to prove that an L_2 norm can be used for the optimization. Firstly, inspired by [39], we prove that the entropy of \mathbf{z} is proportional to its log-variance, without dependence on its hypersphere center. For \mathbf{z} with covariance Σ and $\mathbf{z} \subseteq \mathbb{R}^d$, we have,

$$H(\mathbf{z}) = \mathbb{E}[-\log p(\mathbf{z})] \leq \frac{1}{2} \log((2\pi e)^d \det \Sigma), \quad (10)$$

which holds with equality iff \mathbf{z} is jointly Gaussian [9]. Assuming \mathbf{z} follows an isotropic Gaussian, $\mathbf{z} \sim N(\boldsymbol{\mu}, \sigma^2 I)$ with $\sigma > 0$, we get

$$\begin{aligned} H(\mathbf{z}) &= \frac{1}{2} \log((2\pi e)^d \det \sigma^2 I) \\ &= \frac{d}{2} (1 + \log(2\pi\sigma^2)) \propto \log \sigma^2, \end{aligned} \quad (11)$$

which shows that the entropy of \mathbf{z} is proportional to its log-variance for a fixed dimensionality d . The whole process of the proof has no dependence on μ , showing that we can simply set the hypersphere center to the origin point. In this case, the L_2 norm can be used for the optimization of the entropy:

$$\mathcal{L}_{norm} = \frac{1}{N} \sum_{i=1}^N \|\mathbf{z}_i\|_2, \quad (12)$$

which minimizes the empirical variance and thus minimizes the entropy of a latent Gaussian. Note that this is similar to SVDD loss [38], i.e., $\mathcal{L}_{SVDD} = \frac{1}{N} \sum_{i=1}^N \|\mathbf{z}_i - \mathbf{c}\|_2$, except that SVDD loss requires an additional hypersphere center \mathbf{c} and it needs to be determined via a pre-training process. The whole training process thus needs to be split into two stages if use SVDD loss [39]. *We replace the SVDD loss as an L_2 norm in this paper, which eliminates the dependence on the hypersphere center and helps achieve end-to-end training.*

Note that there is a contradiction between the optimization of mutual information and entropy. When the latent representations have extremely low entropy, especially zero in the extreme case, the model can be considered as mapping all data into a constant in which the mutual information is restricted to zero. The value of \mathcal{L}_{norm} collapses to zero when the encoder converges to a constant function. It thus makes the optimization of reconstruction errors extremely difficult. However, it is difficult to balance the optimization of mutual information and entropy with a single hyperparameter. To tackle this problem, we introduce an additional encoder $Enc_2(\cdot)$ that can be considered as a ‘replicate’ of the original encoder. A consistency loss is leveraged to enforce the similarity between the two encoders. This architecture attempts to make the first encoder focuses on optimizing the mutual information, and the second encoder focuses on optimizing the entropy, thus preventing the reconstruction task from being prematurely affected by the L_2 norm loss. In the implementation, the second encoder remaps the reconstruction outputs to the latent space:

$$\hat{\mathbf{z}} = Enc_2(Dec(Enc_1(\mathbf{x}))), \quad (13)$$

where $\hat{\mathbf{z}}$ is the output of the new encoder $Enc_2(\cdot)$. Then we conduct the L_2 norm only to $\hat{\mathbf{z}}$:

$$\mathcal{L}_{norm-semi} = \frac{1}{N+M} \sum_{i=1}^{N+M} (\|\hat{\mathbf{z}}_i\|_2)^{y_i}, y_i \in \{-1, 1\}, \quad (14)$$

where y_i indicates the label of the data ($y_i = -1$ for the labeled outlier samples while $y_i = 1$ for the normal samples). This entropy loss enforces the compacted representation (minimizing $H_n(\mathbf{z})$) for the normal data and scattered representation (maximizing $H_o(\mathbf{z})$) for the labeled outliers. To define the consistency between the two encoders, similar to the assistant loss function [1], we resort to a consis-

tent constraint between their corresponding latent representations:

$$\mathcal{L}_{ass-semi} = \frac{1}{N+M} \sum_{i=1}^{N+M} \|\hat{\mathbf{z}}_i - \mathbf{z}_i\|^2. \quad (15)$$

The corresponding training architecture, named end-to-end semi-supervised anomaly detection (ESAD), is shown in Figure 1 (b). Different from [1], where two latent spaces learn the same embeddings, two encoders in ESAD focus on different optimization goals, thus showing different results during training (see Section 4.6 for the T-SNE visualization). Finally, we define our training loss as follow:

$$\mathcal{L}_{semi} = \mathcal{L}_{rec-semi} + \lambda_1 \mathcal{L}_{norm-semi} + \lambda_2 \mathcal{L}_{ass-semi}, \quad (16)$$

where λ_1 and λ_2 are two hyperparameters. We will further discuss the impacts of these two hyperparameters in the experiment section. To this end, we achieve end-to-end training for semi-supervised anomaly detection.

3.4. Anomaly Score Measurement

In this part, we discuss how we calculate the anomaly score in the test phase. As discussed in Section 3.2, both the mutual information and the entropy are related to the performance of anomaly detection. We thus use both $\mathcal{L}_{rec-semi}$ and $\mathcal{L}_{norm-semi}$ to measure the anomaly score for the given samples, since they are related to the mutual information and the entropy, respectively. In the test phase, we calculate the reconstruction error of each input sample \mathbf{x} and the value of L_2 norm for its representation $\hat{\mathbf{z}}$ for anomaly detection. The anomaly score is formulated as:

$$\mathcal{S}_{test} = \|\hat{\mathbf{x}} - \mathbf{x}\|^2 + \lambda_1 \|\hat{\mathbf{z}}\|_2, \quad (17)$$

where λ_1 is the same as the setting in the training process. We will further discuss the impact of λ_1 in Section 4.5.

To the best of our knowledge, it is the first time considering both the terms of the mutual information and the entropy for the anomaly score measurement. On the contrary, most one-class classification based methods, e.g., OC-SVM [43], only consider the term of the entropy. Similarly, Deep SVDD [38] and Deep SAD [39] also consider only the term of the entropy, since they only use the SVDD loss as the final anomaly score. Most reconstruction based methods or restoration based methods, including the vanilla AE [26] and ARNet [53], only consider the term of mutual information, since they only use the reconstruction or restoration loss as the anomaly score. Results show that considering both of the two terms significantly improves the performance of anomaly detection.

4. Experiments

In this section, we conduct substantial experiments to validate our method. The ESAD is first evaluated on mul-

multiple benchmark datasets under the standard AUC metric, comparing with several state-of-the-arts. Then the sensitivity is analyzed to show the stability of ESAD. We also present the respective effects of different designs through ablation study. Finally, we visualize the latent representations of ESAD through T-SNE.

4.1. Experimental Setups

4.1.1 Datasets

We conduct semi-supervised anomaly detection experiments on three popular natural image datasets [23, 51, 22], together with six non-image classic anomaly detection datasets [37], all following the settings in [39]. To validate our method on real-world anomaly detection scenarios, i.e., with higher resolution and with more complex anomalies, we additionally conduct experiments on two medical image datasets [4, 49]. For all datasets, the training and testing partitions remain as default. We introduce these datasets briefly as follows:

Natural Image Datasets. MNIST [23], a dataset consists of 70,000 28×28 handwritten grayscale digit images; Fashion-MNIST [51], a relatively new dataset comprising 28×28 grayscale images of 70,000 fashion products from 10 categories, with 7,000 images per category; CIFAR-10 [22], a dataset consists of 60,000 32×32 RGB images of 10 classes, with 6,000 images for per class.

Medical Image Datasets. Following [44, 47], we examine the detection of metastases in H&E stained images of lymph nodes in Camelyon16 [4] and the recognition of fourteen diseases on the chest X-rays in the NIH dataset [49].

Classic anomaly detection benchmark datasets. We use six non-image classic anomaly detection benchmark datasets [37]. Following [39], for the evaluation, we consider random train-to-test set splits of 60:40 while maintaining the original proportion of anomalies in each set.

4.1.2 Evaluation Protocols

We quantify the model performance using the area under the Receiver Operating Characteristic (ROC) curve metric (AUC). It is commonly adopted as performance measurement in anomaly detection tasks and eliminates the subjective decision of threshold value to divide the normal samples from the anomalous ones.

4.2. Experiments on Natural Images

Competing Methods. We consider several shallow unsupervised methods, deep unsupervised anomaly detection competitors and semi-supervised anomaly detection approaches as baselines. For the shallow unsupervised methods, OC-SVM [43] and Isolation Forest [24] are considered. For the deep unsupervised anomaly detection competitors, we consider CAE [26], Deep SVDD [38]

Table 1. Results of anomaly detection on natural image datasets, where we increase the ratio of labeled anomalies γ_l in the training set. We report the avg. AUC with st. dev. computed over 90 experiments at various ratios γ_l .

Data	γ_l	SSAD Hybrid [19]	SS-DGM [20]	Deep SAD [39]	ESAD (ours)
MNIST	.00	96.3 \pm 2.5		92.8 \pm 4.9	98.5 \pm 1.3
	.01	96.8 \pm 2.3	89.9 \pm 9.2	96.4 \pm 2.7	99.2 \pm 0.7
	.05	97.4 \pm 2.0	92.2 \pm 5.6	96.7 \pm 2.4	99.4 \pm 0.3
	.10	97.6 \pm 1.7	91.6 \pm 5.5	96.9 \pm 2.3	99.5 \pm 0.4
	.20	97.8 \pm 1.5	91.2 \pm 5.6	96.9 \pm 2.4	99.6 \pm 0.3
F-MNIST	.00	91.2 \pm 4.7		89.2 \pm 6.2	94.0 \pm 4.5
	.01	89.4 \pm 6.0	65.1 \pm 16.3	90.0 \pm 6.4	95.3 \pm 4.2
	.05	90.5 \pm 5.9	71.4 \pm 12.7	90.5 \pm 6.5	95.6 \pm 4.1
	.10	91.0 \pm 5.6	72.9 \pm 12.2	91.3 \pm 6.0	95.8 \pm 4.0
	.20	89.7 \pm 6.6	74.7 \pm 13.5	91.0 \pm 5.5	95.9 \pm 4.0
CIFAR-10	.00	63.8 \pm 9.0		60.9 \pm 9.4	78.8 \pm 6.5
	.01	70.5 \pm 8.3	49.7 \pm 1.7	72.6 \pm 7.4	83.7 \pm 6.4
	.05	73.3 \pm 8.4	50.8 \pm 4.7	77.9 \pm 7.2	86.9 \pm 6.8
	.10	74.0 \pm 8.1	52.0 \pm 5.5	79.8 \pm 7.1	87.8 \pm 6.7
	.20	74.5 \pm 8.0	53.2 \pm 6.7	81.9 \pm 7.0	88.5 \pm 6.9

Table 2. Average area under the ROC curve (AUC) in % on natural image datasets, comparing with unsupervised anomaly detection methods. “†” denotes the highest test AUC among multiple running for the strong baselines. “*” denotes the highest test AUC among all training epochs for the stronger baselines. Besides the full version of ESAD, we also report the unsupervised version of ESAD, where we ignore the labeled outlier data in the training set.

Method	MNIST	F-MNIST	CIFAR-10
CAE [26]	92.9 \pm 5.7	90.2 \pm 5.8	56.2 \pm 13.2
IF Hybrid [24]	90.5 \pm 5.3	82.5 \pm 8.1	59.9 \pm 6.7
Deep SVDD [38]	92.8 \pm 4.9	89.2 \pm 6.2	60.9 \pm 9.4
AnoGAN† [42]	93.7	-	61.2
ALOCC* [40]	93.3	-	62.2
ADGAN* [11]	94.7	88.4	62.4
OC-SVM Hybrid [43]	96.3 \pm 2.5	91.2 \pm 4.7	63.8 \pm 9.0
OCGAN† [33]	97.5	-	65.6
GANomaly* [2]	92.8	80.9	69.5
P-KDGAN† [55]	97.8	-	73.8
DGEO† [17]	98.0	93.5	86.0
ESAD (unsupervised)	98.5 \pm 1.3	94.0 \pm 4.5	78.8 \pm 6.5
ESAD (full)	99.6 \pm 0.3	95.9 \pm 4.0	88.5 \pm 6.9

AnoGAN [42], ALOCC [40], ADGAN [11], OCGAN [33], GANomaly [2], P-KDGAN [55] and DGEO [17]. For the semi-supervised anomaly detection approaches, we consider SSAD [19], SS-DGM [20] and Deep SAD [39]. OC-SVM and SSAD here have unfair advantages by selecting their hyperparameters to maximize AUC on a subset (10%) of the test set to establish a strong baseline. More details are shown in the supplementary material.

Experiment Settings. For a dataset with C classes, we conduct a batch of C experiments respectively with each of the C classes set as the normal class once. We then evaluate performance on an independent test set, which contains samples from all classes, including normal and anomalous

data. As all classes have equal volumes of samples, the overall number proportion of normal and anomalous samples is $1 : C - 1$. For ESAD, the hyperparameter λ_1 and λ_2 are set to 1 as default. The architecture of the autoencoder and the data preprocessing is aligned with [53]. We give the full details in the supplementary material.

Comparison with State-of-the-art Methods. The effectiveness of adding labeled anomalies during training is investigated in this part. By adding labeled outlier samples x_1, \dots, x_M with $y_j = -1$ to the training set, we increase the ratio of labeled training data $\gamma_l = M/(N + M)$. The number of anomaly classes included in the labeled training data is set to 1, i.e., there are still eight unseen classes at testing time. We iterate this training set generation process and report the average results over the ten kinds of normal classes \times nine labeled outlier classes, i.e. over 90 experiments per labeled ratio γ_l . The corresponding results are shown in Table 1. On all involved datasets, results present that the average AUCs of ESAD outperform all other methods. Results when $\gamma_l > 0$ are much better than the results when $\gamma_l = 0$, showing the effectiveness of the semi-supervised training scheme.

Comparison with Unsupervised Methods. To obtain a fair comparison with unsupervised anomaly detection methods, we train ESAD without the labeled outlier data, thus ESAD degenerates in an unsupervised fashion. Table 2 shows the anomaly detection performance of ESAD under unsupervised training conditions, comparing with several state-of-the-art unsupervised anomaly detection methods. Results show that ESAD (unsupervised) outperforms all baselines on MNIST and F-MNIST, while only performs worse than DGEO [17] on CIFAR-10. However, DGEO has many assumptions for the training data, e.g., the images should have deterministically orientation. This makes DGEO perform poorly in more realistic anomaly detection datasets, such as medical images (see Section 4.3).

4.3. Experiments on Medical Images

Medical images, such as H&E stained images, X-ray, etc., have extremely high resolution compared to natural images. At the same time, the patient’s lesions may only occupy a small part of the entire image, which brings great challenges to anomaly detection. To validate the anomaly detection performance of ESAD on real-world anomaly detection scenarios, in this section, we examined two challenging medical problems with different image characteristics and abnormality appearance, i.e., Camelyon16 [4] and chest X-rays in NIH [49]. We consider several state-of-the-arts as the baselines, including DAOL [44], DGEO [17], PIAD [46], DIF [32] Deep SAD [39], and DPA [47]. Note that for the unsupervised baselines [17, 46, 32], the anomalous samples in the training set are used for validation.

Anomaly Detection on Chest X-Rays. NIH images with-

Table 3. Performance of anomaly detection methods on medical image datasets. We report the avg. AUC in % with st. dev. computed over 3 runs.

Method	Cam.16	NIH (a sub.)	NIH (PA)	NIH (AP)
DAOL [44]	-	80.5 \pm 2.1	-	-
DGEO [17]	45.9 \pm 2.1	85.3 \pm 1.0	63.6 \pm 0.6	54.4 \pm 0.6
PIAD [46]	89.5 \pm 0.6	87.3 \pm 0.9	68.7 \pm 0.5	58.6 \pm 0.3
DIF [32]	90.6 \pm 0.3	85.3 \pm 0.4	47.2 \pm 0.4	56.1 \pm 0.2
Deep SAD [39]	92.1 \pm 0.4	90.9 \pm 0.2	51.9 \pm 0.8	59.8 \pm 0.1
DPA [47]	93.4 \pm 0.3	92.6 \pm 0.2	70.8 \pm 0.1	58.5 \pm 0.0
ESAD	96.8 \pm 0.4	94.6 \pm 0.4	68.9 \pm 0.2	60.1 \pm 0.2

out any disease marker were considered normal. Pulmonary and cardiac abnormalities in this dataset include atelectasis, effusion, infiltration, mass, nodule, pneumonia, pneumothorax, consolidation, edema, emphysema, fibrosis, pleural thickening, hernia and cardiomegaly, which are both considered anomalous. Following [44, 47], we split the dataset into two sub-datasets having only posteroanterior (PA) or anteroposterior (AP) projections. Note that in the training set, the ratios of labeled outlier samples are 3.9% for AP and 3.3% for PA. The labeled outlier samples contain only the most frequent disease (‘Infiltration’) out of fourteen possibilities. It means that there are still thirteen unseen possibilities of anomalies in the test set. We also experiment on a subset containing clearer normal/anomalous cases [44]. This subset consists of 5110 normal and 857 anomalous images for training, and 677 normal and 677 anomalous images for testing. Default preprocessing of chest X-rays involved a 768×768 central crop and resize to 64×64 . Comparing with the subset in [44], abnormality in PA and AP may occupy a smaller region of lungs, or be almost invisible when the images are resized to 64×64 , thus bring a greater challenge for anomaly detection.

As shown in Table 3, the anomaly detection performance of ESAD outperforms all state-of-the-art methods on the clearer subset [44] and AP subset. DPA [47] performs better than ESAD on the subset of PA. Note that DPA uses a higher resolution version of the images (256×256) for validation, so it has a greater advantage comparing with other methods.

Metastases Detection in Digital Pathology. For the Camelyon16 Challenge [4], we sample the Vahadane-normalized [48] 64×64 tiles from the fully normal slides with magnification of $10\times$, and treat these as normal. Tiles with metastases are treated as anomalous. It contains 7612 normal and 200 anomalous training images, and 4000 (normal) + 817 (anomalous) images for the test. As shown in Table 3, the anomaly detection performance of ESAD outperforms all state-of-the-art methods. Note that DPA [47] uses higher resolution version of the images (256×256) for validation. In addition, DGEO [17] shows poor performance on the digital pathology data, since the images are invariant to geometric transformations. Indeed, digital

Table 4. Results on classic anomaly detection benchmark datasets in the setting with a ratio of labeled anomalies of $\gamma_l = 0.01$. We report the avg. AUC with st. dev. computed over 10 seeds.

Data	OC-SVM Hybrid [43]	CAE [26]	Deep SVDD [38]	SSAD Hybrid [19]	SS-DGM [20]	Deep SAD [39]	ESAD (ours)	Supervised Classifier
arrhythmia	76.7 \pm 6.2	74.0 \pm 7.5	74.6 \pm 9.0	78.3 \pm 5.1	50.3 \pm 9.8	75.9 \pm 8.7	85.2 \pm 2.9	39.2 \pm 9.5
cardio	82.8 \pm 9.3	94.3 \pm 2.0	84.8 \pm 3.6	86.3 \pm 5.8	66.2 \pm 14.3	95.0 \pm 1.6	98.8 \pm 0.5	83.2 \pm 9.6
satellite	68.6 \pm 4.8	80.0 \pm 1.7	79.8 \pm 4.1	86.9 \pm 2.8	57.4 \pm 6.4	91.5 \pm 1.1	92.5 \pm 0.7	87.2 \pm 2.1
satimage-2	96.7 \pm 2.1	99.9 \pm 0.0	98.3 \pm 1.4	96.8 \pm 2.1	99.2 \pm 0.6	99.9 \pm 0.1	99.9 \pm 0.1	99.9 \pm 0.1
shuttle	94.1 \pm 9.5	98.2 \pm 1.2	86.3 \pm 7.5	97.7 \pm 1.0	97.9 \pm 0.3	98.4 \pm 0.9	99.1 \pm 1.1	95.1 \pm 8.0
thyroid	91.2 \pm 4.0	75.2 \pm 10.2	72.0 \pm 9.7	95.3 \pm 3.1	72.7 \pm 12.0	98.6 \pm 0.9	99.6 \pm 0.2	97.8 \pm 2.6

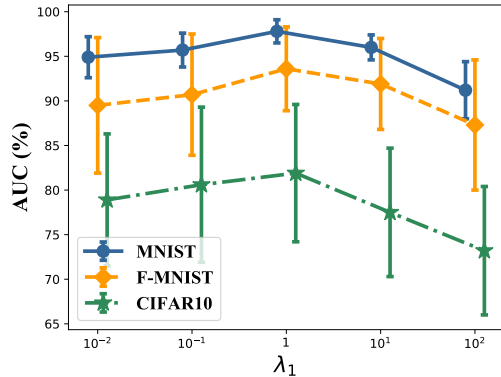


Figure 2. ESAD sensitivity analysis w.r.t. λ_1 . We report avg. AUC with st. dev. over 90 experiments for various values of hyperparameter λ_1 . Best viewed in color.

Table 5. Ablation study on different designs for ESAD on classic anomaly detection benchmark datasets. The “ 2^{nd} encoder” means whether we add the second encoder for ESAD. “Gaussian” and “Permutation” are two different transformed versions of labeled outliers for the supervision of the reconstruction task. Note that Per. means random permutation between various dimensions.

2^{nd} encoder	$\mathcal{L}_{ass-semi}$	Gaussian	Permutation	satellite	cardio
\times	\times	\times	\times	87.9 \pm 1.7	96.5 \pm 1.1
\checkmark	\times	\times	\times	90.0 \pm 1.2	97.2 \pm 0.9
\checkmark	\checkmark	\times	\times	90.4 \pm 1.1	97.9 \pm 1.0
\checkmark	\checkmark	\checkmark	\times	92.0 \pm 1.1	98.2 \pm 0.6
\checkmark	\checkmark	\times	\checkmark	92.5 \pm 1.0	98.6 \pm 0.6
\checkmark	\checkmark	\checkmark	\checkmark	92.5 \pm 0.7	98.8 \pm 0.5

pathology scans do not have space orientation; rotations and translations of them are not distinguishable.

4.4. Experiments on Classic Anomaly Detection Benchmark Datasets

We examine the anomaly detection performance of the various methods on well-established classic anomaly detection benchmark datasets [37] with $\gamma_l = 0.01$. The corresponding results are shown in Table 4. Comparing with other state-of-the-arts, ESAD shows the highest AUCs and stability. It shows that unlike other deep approaches [14, 21, 27, 12, 17], ESAD is not domain or data-type specific.

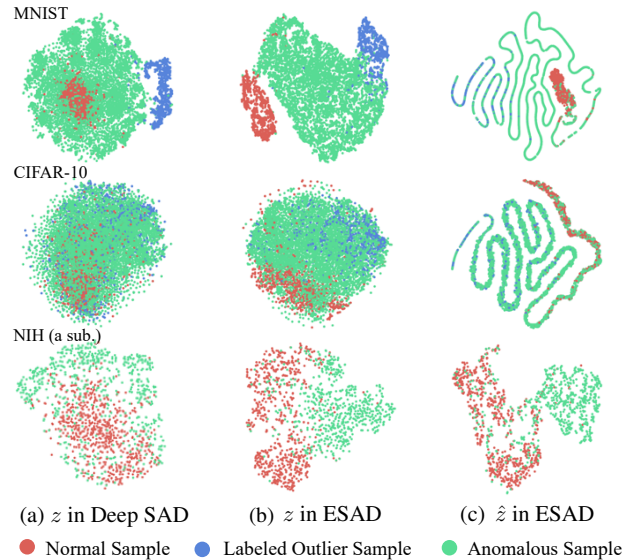


Figure 3. T-SNE visualization of latent representations on MNIST (top), CIFAR-10 (middle) and NIH (bottom). Best viewed in color.

4.5. Sensitivity Analysis and Ablation Study

We analyze the sensitivity of the major hyperparameters of ESAD. According to Eq. (16), there are two hyperparameters, λ_1 and λ_2 . λ_1 has a certain impact on the performance of semi-supervised anomaly detection. The larger λ_1 means more attention is paid to the optimization of entropy, while the smaller λ_1 pays more attention to the mutual information. Figure 2 shows the performance with different λ_1 using ESAD. The results show that the best AUC can be obtained when λ_1 is set to 1 in all the three datasets. When λ_1 is relatively too small or too large, relatively poor anomaly detection performance will be achieved. Fortunately, the relationship between AUCs and the λ_1 presents the same pattern in all datasets, which means that when changing datasets, we may not need to spend too many resources on the adjustment of λ_1 . For λ_2 , we found through experiments that modifying λ_2 has a relatively small impact unless λ_2 is too large. We thus set λ_2 always to 1. More details are shown in the supplementary material.

The model architecture and different transforming strategies for outlier samples are discussed in Table 5 through

ablation studies. Experiments are conducted on the classic benchmark datasets, i.e., cardio and satellite. Results show that without the second encoder, ESAD shows relatively low and unstable AUCs (the entropy loss is conducted on the first encoder in this case). For the transforming strategies, when directly using the original data as supervision, ESAD also attains relatively low AUCs. When the supervision is changed and $\tilde{\mathbf{x}} \neq \mathbf{x}$ (whether adding Gaussian noise or introducing random permutation between various dimensions), the AUCs are relatively higher.

4.6. Visualization Analysis

We show that the latent representations extracted by ESAD can better be used to distinguish samples of different categories through T-SNE [25] analysis. We conduct experiments on MNIST, CIFAR-10 and the medical image dataset NIH. Figure 3 (a) shows the results using latent representations extracted by Deep SAD. Figure 3 (b) and (c) visualize different latent representations, i.e., z and \hat{z} , extracted by ESAD, which are more discriminative than the baseline. In Figure 3 (c), \hat{z} shows a more specific structure. It shows that the two latent representations have learned different information.

5. Conclusion

In this paper, under the information theoretic framework, we show that factors of *mutual information* and *entropy* constitute an integral objective function for anomaly detection. We achieve end-to-end training by proposing a novel model architecture. The proposed information theoretic framework can also be applied to more semi-supervised tasks, opening avenues for future research.

References

- [1] S. Akcay, A. Atapour-Abarghouei, and T. P. Breckon. GANomaly: Semi-Supervised Anomaly Detection via Adversarial Training. In *Asian Conference on Computer Vision (ACCV)*, 2018. 2, 5
- [2] Samet Akçay, Amir Atapour-Abarghouei, and Toby P Breckon. Skip-ganomaly: Skip connected and adversarially trained encoder-decoder anomaly detection. *International Joint Conference on Neural Networks (IJCNN)*, 2019. 6
- [3] Jinwon An and Sungzoon Cho. Variational autoencoder based anomaly detection using reconstruction probability. *Special Lecture on IE*, 2015. 2
- [4] Babak Ehteshami Bejnordi, Mitko Veta, Paul Johannes Van Diest, Bram Van Ginneken, Nico Karssemeijer, Geert Litjens, Jeroen AWM Van Der Laak, Meyke Hermesen, Quirine F Manson, Maschenka Balkenhol, et al. Diagnostic assessment of deep learning algorithms for detection of lymph node metastases in women with breast cancer. *Jama*, 2017. 2, 3, 6, 7, 14, 15
- [5] Léon Bottou. Large-scale machine learning with stochastic gradient descent. In *Proceedings of COMPSTAT'2010*. 2010. 12
- [6] Varun Chandola, Arindam Banerjee, and Vipin Kumar. Anomaly detection: A survey. *ACM computing surveys (CSUR)*, 2009. 1
- [7] Olivier Chapelle, Bernhard Scholkopf, and Alexander Zien. Semi-supervised learning. *IEEE Transactions on Neural Networks*, 2009. 3
- [8] Thomas M Cover and Joy A Thomas. Elements of information theory 2nd edition (Wiley series in Telecommunications and Signal Processing), 2006. 12
- [9] Thomas M Cover and Joy A Thomas. *Elements of information theory*. John Wiley & Sons, 2012. 4
- [10] Zihang Dai, Zhilin Yang, Fan Yang, William W Cohen, and Russ R Salakhutdinov. Good semi-supervised learning that requires a bad gan. In *Advances in Neural Information Processing Systems (NeurIPS)*, 2017. 3
- [11] Lucas Deecke, Robert Vandermeulen, Lukas Ruff, Stephan Mandt, and Marius Kloft. Anomaly detection with generative adversarial networks. *arXiv preprint arXiv:1809.04758*, 2018. 6
- [12] Lucas Deecke, Robert Vandermeulen, Lukas Ruff, Stephan Mandt, and Marius Kloft. Image anomaly detection with generative adversarial networks. In *Joint european conference on machine learning and knowledge discovery in databases*, 2018. 2, 8
- [13] Vincent Dumoulin, Ishmael Belghazi, Ben Poole, Olivier Mastropietro, Alex Lamb, Martin Arjovsky, and Aaron Courville. Adversarially learned inference. In *International Conference on Learning Representations (ICLR)*, 2017. 12
- [14] Tolga Ergen, Ali Mirza, and Suleyman Kozat. Unsupervised and semi-supervised anomaly detection with lstm neural networks. *IEEE Transactions on Neural Networks and Learning Systems (TNNLS)*, 2017. 3, 8
- [15] Eleazar Eskin. Anomaly detection over noisy data using learned probability distributions. In *International Conference on Machine Learning (ICML)*, 2000. 2
- [16] Kevin Eykholt, Ivan Evtimov, Earlene Fernandes, Bo Li, Amir Rahmati, Chaowei Xiao, Atul Prakash, Tadayoshi Kohno, and Dawn Song. Robust physical-world attacks on deep learning visual classification. In *Proceedings of the IEEE/CVF Conference on Computer Vision and Pattern Recognition (CVPR)*, 2018. 1
- [17] Izhak Golan and Ran El-Yaniv. Deep anomaly detection using geometric transformations. In *Advances in Neural Information Processing Systems (NeurIPS)*, 2018. 2, 6, 7, 8
- [18] Dong Gong, Lingqiao Liu, Vuong Le, Budhaditya Saha, Moussa Reda Mansour, Svetha Venkatesh, and Anton van den Hengel. Memorizing normality to detect anomaly: Memory-augmented deep autoencoder for unsupervised anomaly detection. In *Proceedings of the IEEE international conference on computer vision (ICCV)*, 2019. 2
- [19] Nico Görnitz, Marius Kloft, Konrad Rieck, and Ulf Brefeld. Toward supervised anomaly detection. *Journal of Artificial Intelligence Research*, 2013. 1, 3, 6, 8, 13, 14

- [20] Durk P Kingma, Shakir Mohamed, Danilo Jimenez Rezende, and Max Welling. Semi-supervised learning with deep generative models. In *Advances in Neural Information Processing Systems (NeurIPS)*, 2014. 3, 6, 8, 13, 14
- [21] B Ravi Kiran, Dilip Mathew Thomas, and Ranjith Parakkal. An overview of deep learning based methods for unsupervised and semi-supervised anomaly detection in videos. *Journal of Imaging*, 2018. 3, 8
- [22] Alex Krizhevsky and Geoffrey Hinton. Learning multiple layers of features from tiny images. Technical report, Cite-seer, 2009. 2, 6
- [23] Yann LeCun. The mnist database of handwritten digits. <http://yann.lecun.com/exdb/mnist/>, 1998. 2, 6
- [24] Fei Tony Liu, Kai Ming Ting, and Zhi-Hua Zhou. Isolation forest. In *The IEEE International Conference on Data Mining (ICDM)*, 2008. 6, 13, 14
- [25] Laurens van der Maaten and Geoffrey Hinton. Visualizing data using t-sne. *Journal of machine learning research*, 2008. 2, 9
- [26] Jonathan Masci, Ueli Meier, Dan Cireşan, and Jürgen Schmidhuber. Stacked convolutional auto-encoders for hierarchical feature extraction. In *International Conference on Artificial Neural Networks (ICANN)*, 2011. 5, 6, 8, 13, 14
- [27] Erxue Min, Jun Long, Qiang Liu, Jianjing Cui, Zhiping Cai, and Junbo Ma. Su-ids: A semi-supervised and unsupervised framework for network intrusion detection. In *International Conference on Cloud Computing and Security*, 2018. 3, 8
- [28] Jordi Muñoz-Marí, Francesca Bovolo, Luis Gómez-Chova, Lorenzo Bruzzone, and Gustavo Camp-Valls. Semisupervised one-class support vector machines for classification of remote sensing data. *IEEE transactions on geoscience and remote sensing*, 2010. 1
- [29] Miguel Nicolau, James McDermott, and Van Loi Cao. A hybrid autoencoder and density estimation model for anomaly detection. In *International Conference on Parallel Problem Solving from Nature*. Springer, 2016. 2
- [30] Augustus Odena. Semi-supervised learning with generative adversarial networks. *arXiv preprint arXiv:1606.01583*, 2016. 3
- [31] Avital Oliver, Augustus Odena, Colin A Raffel, Ekin Dogus Cubuk, and Ian Goodfellow. Realistic evaluation of deep semi-supervised learning algorithms. In *Advances in Neural Information Processing Systems (NeurIPS)*, 2018. 3
- [32] Khalil Ouardini, Huijuan Yang, Balagopal Unnikrishnan, Manon Romain, Camille Garcin, Houssam Zenati, J Peter Campbell, Michael F Chiang, Jayashree Kalpathy-Cramer, Vijay Chandrasekhar, et al. Towards practical unsupervised anomaly detection on retinal images. In *Domain Adaptation and Representation Transfer and Medical Image Learning with Less Labels and Imperfect Data*. Springer, 2019. 7
- [33] Pramuditha Perera, Ramesh Nallapati, and Bing Xiang. Ocgan: One-class novelty detection using gans with constrained latent representations. In *Proceedings of the IEEE/CVF Conference on Computer Vision and Pattern Recognition (CVPR)*, 2019. 1, 4, 6
- [34] Clifton Phua, Vincent Lee, Kate Smith, and Ross Gayler. A comprehensive survey of data mining-based fraud detection research. *arXiv preprint arXiv:1009.6119*, 2010. 1
- [35] Mostafa Rahmani and George K. Atia. Coherence pursuit: Fast, simple, and robust principal component analysis. *IEEE Transactions on Signal Processing*, 2017. 2
- [36] Antti Rasmus, Mathias Berglund, Mikko Honkala, Harri Valpola, and Tapani Raiko. Semi-supervised learning with ladder networks. In *Advances in Neural Information Processing Systems (NeurIPS)*, 2015. 3
- [37] Shebuti Rayana. Odds library. <http://odds.cs.stonybrook.edu>, 2016. 2, 6, 8, 12
- [38] Lukas Ruff, Robert Vandermeulen, Nico Goernitz, Lucas Deecke, Shoaib Ahmed Siddiqui, Alexander Binder, Emmanuel Müller, and Marius Kloft. Deep one-class classification. In *International Conference on Machine Learning (ICML)*, 2018. 2, 3, 5, 6, 8, 13, 14
- [39] Lukas Ruff, Robert A Vandermeulen, Nico Görnitz, Alexander Binder, Emmanuel Müller, Klaus-Robert Müller, and Marius Kloft. Deep semi-supervised anomaly detection. In *International Conference on Learning Representations (ICLR)*, 2020. 1, 2, 3, 4, 5, 6, 7, 8, 13, 14
- [40] Mohammad Sabokrou, Mohammad Khalooei, Mahmood Fathy, and Ehsan Adeli. Adversarially learned one-class classifier for novelty detection. In *Proceedings of the IEEE/CVF Conference on Computer Vision and Pattern Recognition (CVPR)*, 2018. 1, 2, 6
- [41] Mayu Sakurada and Takehisa Yairi. Anomaly detection using autoencoders with nonlinear dimensionality reduction. In *Mlsda Workshop on Machine Learning for Sensory Data Analysis*, 2014. 2
- [42] Thomas Schlegl, Philipp Seeböck, Sebastian M Waldstein, Ursula Schmidt-Erfurth, and Georg Langs. Unsupervised anomaly detection with generative adversarial networks to guide marker discovery. In *International Conference on Information Processing in Medical Imaging*, 2017. 2, 6
- [43] Bernhard Schölkopf, John C Platt, John Shawe-Taylor, Alex J Smola, and Robert C Williamson. Estimating the support of a high-dimensional distribution. *Neural computation*, 2001. 2, 5, 6, 8, 13, 14
- [44] Yu-Xing Tang, You-Bao Tang, Mei Han, Jing Xiao, and Ronald M Summers. Deep adversarial one-class learning for normal and abnormal chest radiograph classification. In *Medical Imaging 2019: Computer-Aided Diagnosis*, 2019. 6, 7
- [45] David MJ Tax and Robert PW Duin. Support vector data description. *Machine learning*, 2004. 1, 13
- [46] Nina Tuluptceva, Bart Bakker, Irina Fedulova, and Anton Konushin. Perceptual image anomaly detection. In *Asian Conference on Pattern Recognition*, 2019. 7
- [47] Nina Tuluptceva, Bart Bakker, Irina Fedulova, Heinrich Schulz, and Dmitry V Dylov. Anomaly detection with deep perceptual autoencoders. *arXiv preprint arXiv:2006.13265*, 2020. 1, 3, 6, 7
- [48] Abhishek Vahadane, Tingying Peng, Amit Sethi, Shadi Albarqouni, Lichao Wang, Maximilian Baust, Katja Steiger, Anna Melissa Schlitter, Irene Esposito, and Nassir Navab. Structure-preserving color normalization and sparse stain separation for histological images. *IEEE transactions on medical imaging*, 2016. 7

- [49] Xiaosong Wang, Yifan Peng, Le Lu, Zhiyong Lu, Mohammadhadi Bagheri, and Ronald M Summers. Chestx-ray8: Hospital-scale chest x-ray database and benchmarks on weakly-supervised classification and localization of common thorax diseases. In *Proceedings of the IEEE conference on computer vision and pattern recognition (CVPR)*, 2017. 2, 3, 6, 7, 14, 15
- [50] Yan Xia, Xudong Cao, Fang Wen, Gang Hua, and Jian Sun. Learning discriminative reconstructions for unsupervised outlier removal. In *Proceedings of the IEEE international conference on computer vision (ICCV)*, 2015. 2
- [51] Han Xiao, Kashif Rasul, and Roland Vollgraf. Fashion-mnist: a novel image dataset for benchmarking machine learning algorithms. *arXiv preprint arXiv:1708.07747*, 2017. 2, 6
- [52] Huan Xu, C Caramanis, and S Sanghavi. Robust pca via outlier pursuit. *IEEE Transactions on Information Theory*, 2012. 2
- [53] Fei Ye, Chaoqin Huang, Jinkun Cao, Maosen Li, Ya Zhang, and Cewu Lu. Attribute restoration framework for anomaly detection. *arXiv preprint arXiv:1911.10676v2*, 2020. 2, 5, 7
- [54] Jianpeng Zhang, Yutong Xie, Zhibin Liao, Guansong Pang, Johan Verjans, Wenxin Li, Zongji Sun, Jian He, and Chunhua Shen Yi Li. Viral pneumonia screening on chest x-ray images using confidence-aware anomaly detection. *arXiv preprint arXiv:2003.12338*, 2020. 3
- [55] Zhiwei Zhang, Shifeng Chen, and Lei Sun. P-kdgan: Progressive knowledge distillation with gans for one-class novelty detection. *International Joint Conference on Artificial Intelligence (IJCAI)*, 2020. 1, 6
- [56] Kang Zhou, Yuting Xiao, Jianlong Yang, Jun Cheng, Wen Liu, Weixin Luo, Zaiwang Gu, Jiang Liu, and Shenghua Gao. Encoding structure-texture relation with p-net for anomaly detection in retinal images. *European Conference on Computer Vision (ECCV)*, 2020. 3
- [57] Bo Zong, Qi Song, Martin Renqiang Min, Wei Cheng, Cristian Lumezanu, Daeki Cho, and Haifeng Chen. Deep autoencoding gaussian mixture model for unsupervised anomaly detection. In *International Conference on Learning Representations (ICLR)*, 2018. 2

A. Supplementary Proofs

Proposition 1. *If $\text{KL}[p_n(\mathbf{x}, \mathbf{z})||p_a(\mathbf{x}, \mathbf{z})]$ is maximized, then it is equivalent that $\text{KL}[p_n(\mathbf{x})||p_a(\mathbf{x})]$ and $\text{KL}[p_n(\mathbf{z}|\mathbf{x})||p_a(\mathbf{z}|\mathbf{x})]$ are maximized.*

Proof. The KL divergence for the joint distributions can be decomposed with chain rule [8]:

$$\begin{aligned} & \text{KL}[p_n(\mathbf{x}, \mathbf{z})||p_a(\mathbf{x}, \mathbf{z})] \\ &= \mathbb{E}_{p_n(\mathbf{x}, \mathbf{z})} \left[\log \frac{p_n(\mathbf{x}, \mathbf{z})}{p_a(\mathbf{x}, \mathbf{z})} \right] \\ &= \mathbb{E}_{p_n(\mathbf{x}, \mathbf{z})} \left[\log \frac{p_n(\mathbf{x})}{p_a(\mathbf{x})} + \log \frac{p_n(\mathbf{z}|\mathbf{x})}{p_a(\mathbf{z}|\mathbf{x})} \right] \\ &= \text{KL}[p_n(\mathbf{x})||p_a(\mathbf{x})] + \mathbb{E}_{p_n(\mathbf{x})} [\text{KL}[p_n(\mathbf{z}|\mathbf{x})||p_a(\mathbf{z}|\mathbf{x})]]. \end{aligned} \quad (18)$$

To maximize the KL divergence for the joint distributions, it is equivalent that we maximize the KL divergence for both marginal and conditional distributions [13]. \square

Proposition 2. *Let $I_n(\mathbf{x}, \mathbf{z})$ denotes the mutual information between \mathbf{x} and \mathbf{z} for normal data; $H_n(\mathbf{z})$ denotes the entropy of \mathbf{z} for normal data; $H(p_n(\mathbf{z}|\mathbf{x}), p_a(\mathbf{z}|\mathbf{x}))$ denotes the cross-entropy between $p_n(\mathbf{z}|\mathbf{x})$ and $p_a(\mathbf{z}|\mathbf{x})$; $\text{KL}[p_n(\mathbf{x})||p_a(\mathbf{x})]$ denotes the KL divergence between $p_n(\mathbf{x})$ and $p_a(\mathbf{x})$. To be noted, when the dataset is given, i.e. $p_n(\mathbf{x})$ and $p_a(\mathbf{x})$ are fixed (even though anomalous data is unknown). Then:*

$$\begin{aligned} & \max_{\theta} \text{KL}[p_n(\mathbf{x}, \mathbf{z})||p_a(\mathbf{x}, \mathbf{z})] \\ &= \max_{\theta} \{I_n(\mathbf{x}, \mathbf{z}) - H_n(\mathbf{z}) + \mathbb{E}_{p_n(\mathbf{x})} [H(p_n(\mathbf{z}|\mathbf{x}), p_a(\mathbf{z}|\mathbf{x}))] \\ & \quad + \text{KL}[p_n(\mathbf{x})||p_a(\mathbf{x})]\}. \end{aligned} \quad (19)$$

Proof. The KL divergence can be reformulated as:

$$\begin{aligned} & \max_{\theta} \text{KL}[p_n(\mathbf{x}, \mathbf{z})||p_a(\mathbf{x}, \mathbf{z})] \\ &= \max_{\theta} \mathbb{E}_{p_n(\mathbf{x}, \mathbf{z})} \left[\log \frac{p_n(\mathbf{x}, \mathbf{z})}{p_a(\mathbf{x}, \mathbf{z})} \right] \\ &= \max_{\theta} \mathbb{E}_{p_n(\mathbf{x}, \mathbf{z})} \left[\log \frac{p_n(\mathbf{z}|\mathbf{x}) \cdot p_n(\mathbf{x})}{p_a(\mathbf{z}|\mathbf{x}) \cdot p_a(\mathbf{x})} \right] \\ &= \max_{\theta} \mathbb{E}_{p_n(\mathbf{x}, \mathbf{z})} \left[\log \frac{p_n(\mathbf{z}|\mathbf{x}) \cdot p_n(\mathbf{x}) \cdot p_n(\mathbf{z})}{p_a(\mathbf{z}|\mathbf{x}) \cdot p_a(\mathbf{x}) \cdot p_n(\mathbf{z})} \right] \\ &= \max_{\theta} \mathbb{E}_{p_n(\mathbf{x}, \mathbf{z})} \left[\log \left(\frac{p_n(\mathbf{z}|\mathbf{x})}{p_n(\mathbf{z})} \cdot p_n(\mathbf{z}) \cdot \frac{1}{p_a(\mathbf{z}|\mathbf{x})} \cdot \frac{p_n(\mathbf{x})}{p_a(\mathbf{x})} \right) \right]. \end{aligned}$$

The above formula is decomposed into four components. The first term refers to the mutual information between the original data \mathbf{x} and its latent representation \mathbf{z} for the normal

data:

$$\begin{aligned} & \mathbb{E}_{p_n(\mathbf{x}, \mathbf{z})} \left[\log \frac{p_n(\mathbf{z}|\mathbf{x})}{p_n(\mathbf{z})} \right] \\ &= \mathbb{E}_{p_n(\mathbf{x}, \mathbf{z})} \left[\log \frac{p_n(\mathbf{z}|\mathbf{x}) \cdot p_n(\mathbf{x})}{p_n(\mathbf{x}) \cdot p_n(\mathbf{z})} \right] \\ &= \mathbb{E}_{p_n(\mathbf{x}, \mathbf{z})} \left[\log \frac{p_n(\mathbf{x}, \mathbf{z})}{p_n(\mathbf{x}) \cdot p_n(\mathbf{z})} \right] \\ &= I_n(\mathbf{x}, \mathbf{z}). \end{aligned}$$

The second term refers to the negative entropy of \mathbf{z} with respect to p_n :

$$\mathbb{E}_{p_n(\mathbf{x}, \mathbf{z})} [\log p_n(\mathbf{z})] = -\mathbb{E}_{p_n(\mathbf{z})} \left[\log \frac{1}{p_n(\mathbf{z})} \right] = -H_n(\mathbf{z}).$$

The third term refers to the expected value of the cross entropy between the conditional distributions $p_a(\mathbf{z}|\mathbf{x})$ and $p_n(\mathbf{z}|\mathbf{x})$:

$$\begin{aligned} & \mathbb{E}_{p_n(\mathbf{x}, \mathbf{z})} \left[\log \frac{1}{p_a(\mathbf{z}|\mathbf{x})} \right] \\ &= \mathbb{E}_{p_n(\mathbf{x})} \mathbb{E}_{p_n(\mathbf{z}|\mathbf{x})} [-\log p_a(\mathbf{z}|\mathbf{x})] \\ &= \mathbb{E}_{p_n(\mathbf{x})} [H(p_n(\mathbf{z}|\mathbf{x}), p_a(\mathbf{z}|\mathbf{x}))]. \end{aligned}$$

The fourth term is a constant, since $p_n(\mathbf{x})$ and $p_a(\mathbf{x})$ are fixed:

$$\mathbb{E}_{p_n(\mathbf{x}, \mathbf{z})} \left[\log \frac{p_n(\mathbf{x})}{p_a(\mathbf{x})} \right] = \text{KL}[p_n(\mathbf{x})||p_a(\mathbf{x})] = C.$$

Thus the KL divergence can be reformulated as:

$$\begin{aligned} & \max_{\theta} \text{KL}[p_n(\mathbf{x}, \mathbf{z})||p_a(\mathbf{x}, \mathbf{z})] \\ &= \max_{\theta} \{I_n(\mathbf{x}, \mathbf{z}) - H_n(\mathbf{z}) + \mathbb{E}_{p_n(\mathbf{x})} [H(p_n(\mathbf{z}|\mathbf{x}), p_a(\mathbf{z}|\mathbf{x}))] \\ & \quad + \text{KL}[p_n(\mathbf{x})||p_a(\mathbf{x})]\}. \end{aligned} \quad (20)$$

\square

B. Model Architecture and Training Details

The model architecture for ESAD is shown in Table 6. For the training, we use stochastic gradient descent (SGD) [5] optimizer with default hyperparameters in Pytorch. ESAD is trained using a batch size of 32 for 200 epochs. The learning rate is initially set to 0.1, and is divided by 2 every 50 epoch.

C. Classic anomaly detection benchmarks

The supplementary details of the classic anomaly detection benchmarks [37] are shown in Table 7.

Table 6. Model Structure of ESAD.

Layer	Input	Output
$3 \times 3 \times 64$	$x (3 \times H \times W)$	$x_{0-1} (64 \times H \times W)$
$3 \times 3 \times 64$	x_{0-1}	$x_{0-2} (64 \times H \times W)$
MaxPool	x_{0-2}	$x_{1-1} (64 \times 1/2H \times 1/2W)$
$3 \times 3 \times 128$	x_{1-1}	$x_{1-2} (128 \times 1/2H \times 1/2W)$
$3 \times 3 \times 128$	x_{1-2}	$x_{1-3} (128 \times 1/2H \times 1/2W)$
MaxPool	x_{1-3}	$x_{2-1} (128 \times 1/4H \times 1/4W)$
$3 \times 3 \times 256$	x_{2-1}	$x_{2-2} (256 \times 1/4H \times 1/4W)$
$3 \times 3 \times 256$	x_{2-2}	$x_{2-3} (256 \times 1/4H \times 1/4W)$
MaxPool	x_{2-3}	$x_{3-1} (256 \times 1/8H \times 1/8W)$
$3 \times 3 \times 512$	x_{3-1}	$x_{3-2} (256 \times 1/8H \times 1/8W)$
$3 \times 3 \times 512$	x_{3-2}	$x_{3-3} (256 \times 1/8H \times 1/8W)$
MaxPool	x_{3-3}	$x_{4-1} (256 \times 1/8H \times 1/16W)$
$3 \times 3 \times 512$	x_{4-1}	$x_{4-2} (512 \times 1/16H \times 1/16W)$
$3 \times 3 \times 512$	x_{4-2}	$z (512 \times 1/16H \times 1/16W)$
UpSample	z	$up_{3-1} (512 \times 1/8H \times 1/8W)$
$3 \times 3 \times 256$	up_{3-1}	$up_{3-2} (256 \times 1/8H \times 1/8W)$
$3 \times 3 \times 256$	up_{3-2}	$up_{3-3} (256 \times 1/8H \times 1/8W)$
UpSample	up_{3-3}	$up_{2-1} (256 \times 1/4H \times 1/4W)$
$3 \times 3 \times 128$	up_{2-1}	$up_{2-2} (128 \times 1/4H \times 1/4W)$
$3 \times 3 \times 128$	up_{2-2}	$up_{2-3} (128 \times 1/4H \times 1/4W)$
UpSample	up_{2-3}	$up_{1-1} (128 \times 1/2H \times 1/2W)$
$3 \times 3 \times 64$	up_{1-1}	$up_{1-2} (64 \times 1/2H \times 1/2W)$
$3 \times 3 \times 64$	up_{1-2}	$up_{1-3} (64 \times 1/2H \times 1/2W)$
UpSample	up_{1-3}	$up_{0-1} (64 \times H \times W)$
$3 \times 3 \times 64$	up_{0-1}	$up_{0-2} (64 \times H \times W)$
$3 \times 3 \times 64$	up_{0-2}	$up_{0-3} (64 \times H \times W)$
$3 \times 3 \times 3$	up_{0-3}	$\hat{x} (3 \times H \times W)$
$3 \times 3 \times 64$	\hat{x}	$x_{5-1} (64 \times H \times W)$
$3 \times 3 \times 64$	x_{5-1}	$x_{5-2} (64 \times H \times W)$
MaxPool	x_{5-2}	$x_{6-1} (64 \times 1/2H \times 1/2W)$
$3 \times 3 \times 128$	x_{6-1}	$x_{6-2} (128 \times 1/2H \times 1/2W)$
$3 \times 3 \times 128$	x_{6-2}	$x_{6-3} (128 \times 1/2H \times 1/2W)$
MaxPool	x_{6-3}	$x_{7-1} (128 \times 1/4H \times 1/4W)$
$3 \times 3 \times 256$	x_{7-1}	$x_{7-2} (256 \times 1/4H \times 1/4W)$
$3 \times 3 \times 256$	x_{7-2}	$x_{7-3} (256 \times 1/4H \times 1/4W)$
MaxPool	x_{7-3}	$x_{8-1} (256 \times 1/8H \times 1/8W)$
$3 \times 3 \times 512$	x_{8-1}	$x_{8-2} (256 \times 1/8H \times 1/8W)$
$3 \times 3 \times 512$	x_{8-2}	$x_{8-3} (256 \times 1/8H \times 1/8W)$
MaxPool	x_{8-3}	$x_{9-1} (256 \times 1/8H \times 1/16W)$
$3 \times 3 \times 512$	x_{9-1}	$x_{9-2} (512 \times 1/16H \times 1/16W)$
$3 \times 3 \times 512$	x_{9-2}	$\hat{z} (512 \times 1/16H \times 1/16W)$

Table 7. Classic anomaly detection benchmarks.

Dataset	Numbers	Dimensions	#outliers (%)
arrhythmia	452	274	66 (14.6%)
cardio	1,831	21	176 (9.6%)
satellite	6,435	36	2,036 (31.6%)
satimage-2	5,803	36	71 (1.2%)
shuttle	49,097	9	3,511 (7.2%)
thyroid	3,772	6	93 (2.5%)

D. Competing Methods

We consider several shallow unsupervised methods, deep unsupervised anomaly detection competitors and semi-supervised anomaly detection approaches as baselines. Complete details are shown as follows:

(1) OC-SVM/SVDD [43, 45]: The OC-SVM and SVDD are equivalent for the Gaussian/RBF kernel. OC-SVM/SVDD here have unfair advantages by selecting their hyperparameters to maximize AUC on a subset (10%) of the test set to establish a strong baseline. The RBF scale parameters $\gamma \in \{2^{-7}, 2^{-6}, \dots, 2^2\}$ are considered

and the best performing one is selected. Then the best final results are reported over ν -parameter, where $\nu \in \{0.01, 0.05, 0.1, 0.2, 0.5\}$.

(2) Isolation Forest [24]: The number of trees is set to $t = 100$ and the sub-sampling size is set to $\psi = 256$ as recommended in the original work.

(3) SSAD [19]: SSAD also have the unfair advantages the same as OC-SVM/SVDD. The scale parameters γ of the RBF kernel are selected from $\gamma \in \{2^{-7}, 2^{-6}, \dots, 2^2\}$ and then report the best performing one. Otherwise we set the hyperparameters as recommend by the original authors to $\kappa = 1, \kappa = 1, \eta_u = 1$, and $\eta_l = 1$ [19].

(4) Convolutional Autoencoder (CAE) [26]: The autoencoders are trained on the MSE reconstruction loss that also serves as the anomaly score.

(5) Deep SVDD [38]: Both variants, Soft-Boundary Deep SVDD and One-Class Deep SVDD are considered as unsupervised baselines and always report the better performance as the unsupervised result. For Soft-Boundary Deep SVDD, The radius R on every mini-batch is optimally solved. For Deep SVDD, all the bias terms from a network are removed to prevent a hypersphere collapse as recommended by the authors in the original work [38].

(6) SS-DGM [20]: We consider both the $M2$ and $M1+M2$ model and always report the better performing result. Other settings are following the original work [20].

(7) Deep SAD [39]: The results are borrow from [39]. We set $\lambda = 10^{-6}$ and equally weight the unlabeled and labeled examples by setting $\eta = 1$ if not reported otherwise.

To establish hybrid methods, we apply the OC-SVM, IF, and SSAD to the resulting bottleneck representations given by the respective converged autoencoders. In addition, to complete the full learning spectrum, we also include a fully supervised deep classifier trained on the binary cross-entropy loss.

E. Supplementary Experimental Results

We examine three scenarios [39] in which we vary the following three experimental parameters: (i) γ_l , the ratio of labeled outlier samples in the training data; (ii) γ_p , the ratio of pollution, i.e., unknown anomalies, in the training data, and (iii) the number of anomaly classes k_l included in the labeled training data. For the experimental scenario (i), where the effectiveness of adding labeled anomalies during training is investigated, i.e., increasing γ_l , has been shown in the main paper. In this part, we report the complete results for the experimental scenario (ii) and (iii), which are shown in Table 8 and Table 9, respectively.

For the experimental scenario (ii), where the robustness is investigated in this scenario through adding polluted data. With an increasing pollution ratio γ_p , we pollute the training set with anomalies drawn from all nine anomaly classes. We fix $\gamma_l = 0.05$ in this scenario. We report the average

Table 8. Complete results of experimental scenario (ii), where we pollute the unlabeled part of the training set with (unknown) anomalies. We report the avg. AUC with st. dev. computed over 90 experiments at various ratios γ_p .

Data	γ_p	OC-SVM Hybrid [43]	IF Hybrid [24]	CAE [26]	Deep SVDD [38]	SSAD Hybrid [19]	SS-DGM [20]	Deep SAD [39]	ESAD (ours)	Supervised Classifier
MNIST	.00	96.3 \pm 2.5	90.5 \pm 5.3	92.9 \pm 5.7	92.8 \pm 4.9	97.4 \pm 2.0	92.2 \pm 5.6	96.7 \pm 2.4	99.4 \pm 0.3	94.5 \pm 4.6
	.01	95.6 \pm 2.5	90.6 \pm 5.0	91.3 \pm 6.1	92.1 \pm 5.1	95.2 \pm 2.3	92.0 \pm 6.0	95.5 \pm 3.3	99.2 \pm 0.6	91.5 \pm 5.9
	.05	93.8 \pm 3.9	89.7 \pm 6.0	87.2 \pm 7.1	89.4 \pm 5.8	89.5 \pm 3.9	91.0 \pm 6.9	93.5 \pm 4.1	98.5 \pm 1.0	86.7 \pm 7.4
	.10	91.4 \pm 5.1	88.2 \pm 6.5	83.7 \pm 8.4	86.5 \pm 6.8	86.0 \pm 4.6	89.7 \pm 7.5	91.2 \pm 4.9	97.8 \pm 1.3	83.6 \pm 8.2
	.20	85.9 \pm 7.6	85.3 \pm 7.9	78.6 \pm 10.3	81.5 \pm 8.4	82.1 \pm 5.4	87.4 \pm 8.6	86.6 \pm 6.6	96.7 \pm 2.0	79.7 \pm 9.4
F-MNIST	.00	91.2 \pm 4.7	82.5 \pm 8.1	90.2 \pm 5.8	89.2 \pm 6.2	90.5 \pm 5.9	71.4 \pm 12.7	90.5 \pm 6.5	95.6 \pm 4.1	76.8 \pm 13.2
	.01	91.5 \pm 4.6	84.9 \pm 7.2	87.1 \pm 7.3	86.3 \pm 6.3	87.8 \pm 6.1	71.2 \pm 14.3	87.2 \pm 7.1	95.5 \pm 4.1	67.3 \pm 8.1
	.05	90.7 \pm 4.9	85.5 \pm 7.2	81.6 \pm 9.6	80.6 \pm 7.1	82.7 \pm 7.8	71.9 \pm 14.3	81.5 \pm 8.5	94.5 \pm 4.5	59.8 \pm 4.6
	.10	89.3 \pm 6.2	85.5 \pm 7.7	77.4 \pm 11.1	76.2 \pm 7.3	79.8 \pm 9.0	72.5 \pm 15.5	78.2 \pm 9.1	93.6 \pm 4.7	56.7 \pm 4.1
	.20	88.1 \pm 6.9	86.3 \pm 7.4	72.5 \pm 12.6	69.3 \pm 6.3	74.3 \pm 10.6	70.8 \pm 16.0	74.8 \pm 9.4	92.5 \pm 4.9	53.9 \pm 2.9
CIFAR-10	.00	63.8 \pm 9.0	59.9 \pm 6.7	56.2 \pm 13.2	60.9 \pm 9.4	73.3 \pm 8.4	50.8 \pm 4.7	77.9 \pm 7.2	86.9 \pm 6.8	63.5 \pm 8.0
	.01	63.8 \pm 9.3	59.9 \pm 6.7	56.2 \pm 13.1	60.5 \pm 9.4	72.8 \pm 8.1	51.1 \pm 4.7	76.5 \pm 7.2	86.5 \pm 6.9	62.9 \pm 7.3
	.05	62.6 \pm 9.2	59.6 \pm 6.4	55.7 \pm 13.3	59.6 \pm 9.8	71.0 \pm 8.4	50.1 \pm 2.9	74.0 \pm 6.9	84.3 \pm 7.4	62.2 \pm 8.2
	.10	62.9 \pm 8.2	59.1 \pm 6.6	55.4 \pm 13.3	58.6 \pm 10.0	69.3 \pm 8.5	50.5 \pm 3.6	71.8 \pm 7.0	81.9 \pm 7.7	60.6 \pm 8.3
	.20	61.9 \pm 8.1	58.3 \pm 6.2	54.6 \pm 13.3	57.0 \pm 10.6	67.9 \pm 8.1	50.1 \pm 1.7	68.5 \pm 7.1	79.8 \pm 8.8	58.5 \pm 6.7

Table 9. Complete results of experimental scenario (iii), where we increase the number of anomaly classes k_l included in the labeled training data. We report the avg. AUC with st. dev. computed over 100 experiments at various numbers k_l .

Data	k_l	OC-SVM Hybrid [43]	IF Hybrid [24]	CAE [26]	Deep SVDD [38]	SSAD Hybrid [19]	SS-DGM [20]	Deep SAD [39]	ESAD (ours)	Supervised Classifier
MNIST	0	91.4 \pm 5.1	88.2 \pm 6.5	83.7 \pm 8.4	86.5 \pm 6.8	91.4 \pm 5.1		86.5 \pm 6.8	92.7 \pm 3.8	
	1					86.0 \pm 4.6	89.7 \pm 7.5	91.2 \pm 4.9	97.8 \pm 1.3	83.6 \pm 8.2
	2					87.7 \pm 3.8	92.8 \pm 5.3	92.0 \pm 3.6	98.2 \pm 0.9	90.3 \pm 4.6
	3					89.8 \pm 3.3	94.9 \pm 4.2	94.7 \pm 2.8	99.1 \pm 0.6	93.9 \pm 2.8
	5					91.9 \pm 3.0	96.7 \pm 2.3	97.3 \pm 1.8	99.3 \pm 0.5	96.9 \pm 1.7
F-MNIST	0	89.3 \pm 6.2	85.5 \pm 7.7	77.4 \pm 11.1	76.2 \pm 7.3	89.3 \pm 6.2		76.2 \pm 7.3	91.2 \pm 5.4	
	1					79.8 \pm 9.0	72.5 \pm 15.5	78.2 \pm 9.1	93.6 \pm 4.7	56.7 \pm 4.1
	2					80.1 \pm 10.5	74.3 \pm 15.4	80.5 \pm 8.2	94.7 \pm 4.6	62.3 \pm 2.9
	3					83.8 \pm 9.4	77.5 \pm 14.7	83.9 \pm 7.4	95.8 \pm 4.8	67.3 \pm 3.0
	5					86.8 \pm 7.7	79.9 \pm 13.8	87.3 \pm 6.4	96.7 \pm 4.3	75.3 \pm 2.7
CIFAR-10	0	62.9 \pm 8.2	59.1 \pm 6.6	55.4 \pm 13.3	86.6 \pm 10.0	62.9 \pm 8.2		58.6 \pm 10.0	73.5 \pm 6.8	
	1					69.3 \pm 8.5	50.5 \pm 3.6	71.8 \pm 7.0	81.9 \pm 7.7	60.6 \pm 8.3
	2					72.3 \pm 7.5	50.3 \pm 2.4	75.2 \pm 6.4	83.8 \pm 6.0	61.0 \pm 6.6
	3					73.3 \pm 7.0	50.0 \pm 0.7	77.5 \pm 5.9	84.9 \pm 8.1	62.7 \pm 6.8
	5					74.2 \pm 6.5	50.0 \pm 1.0	80.4 \pm 4.6	86.7 \pm 7.0	60.9 \pm 4.6

results over 90 experiments per pollution ratio γ_p . The corresponding results are shown in Table 8. Results show that ESAD is least affected by the pollution data and show the best robustness in all the polluted levels.

For the experimental scenario (iii), we increase the number of anomaly classes k_l included in the labeled part of the training set to increase the diversity of labeled outlier data. ESAD shows better performance in this scenario. For example, the AUC of ESAD on CIFAR-10 increases from 81.9% to 86.7% ($\gamma_l = 0.05$, $\gamma_p = 0.1$) when we change k_l from 1 to 5.

Examples Visualization. We illustrate the predictions of our model in Figure 4. Samples are randomly chosen from H&E-stained lymph node of Camelyon16 challenge [4] (top) and chest X-rays of NIH dataset [49] (bottom). These samples and their corresponding scores show that the higher the score, the more likely to be an anomaly.

Sensitivity Analysis on λ_2 . We analyze the sensitivity of ESAD over the hyperparameters λ_2 . Figure 5 shows the performance with different λ_2 using ESAD on MNIST. We set $\gamma_l = 0.05$, $\gamma_p = 0.1$, $k_l = 1$ in this experiment. Results

show that without the assistant loss, i.e., $\lambda_2 = 0$, ESAD shows relatively low and unstable AUCs. ESAD shows best performance when $\lambda_2 = 1$. When λ_2 is too large, ESAD also shows unstable performance. This is because both two encoders will converge into the same constant function if the impact of the assistant loss is much greater than the other two loss functions. It will cause the model hard to reconstruct any data.

Discussion and Comparison. We discuss the relationship and the differences between Deep SAD and ESAD. Comparing to Deep SAD, ESAD achieves end-to-end training for semi-supervised anomaly detection. The importance of end-to-end training is explained by the KL divergence based objective function. In the implementation, under the proposed semi-supervised anomaly detection framework, there are four major changes for ESAD: (1) Replace the SVDD loss with $\mathcal{L}_{norm-semi}$ to eliminate the dependence on the hypersphere center; (2) Use $\mathcal{L}_{rec-semi}$ for training the labeled outlier samples with opposite optimization direction in the task of reconstruction. For the original Deep SAD, the labeled outlier samples cannot be used during the train-

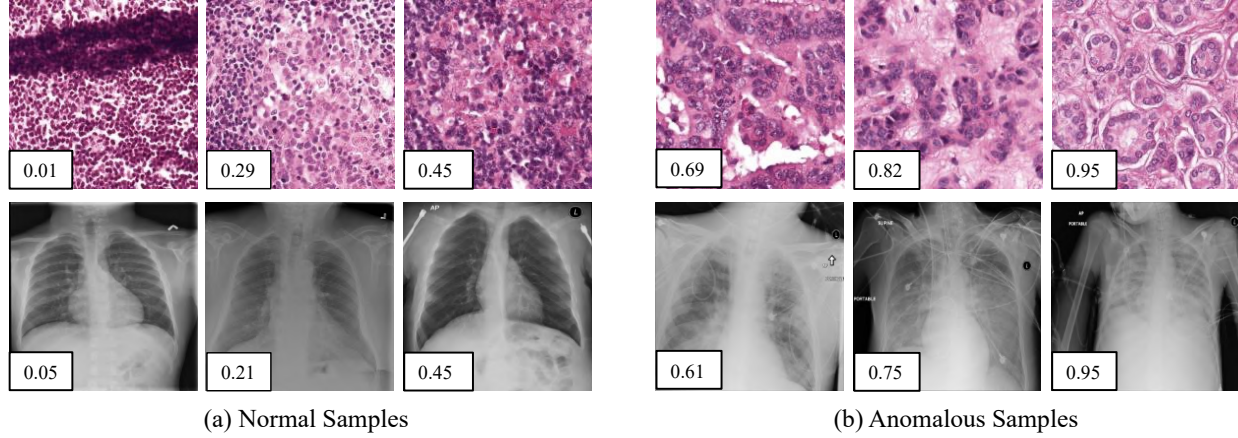


Figure 4. Examples of normal (left) and anomalous (right) samples of H&E-stained lymph node of Camelyon16 challenge [4] (top) and chest X-rays of NIH dataset [49] (bottom). We also showed the predicted anomaly score by the proposed method. The higher the score, the more likely to be an anomaly. Best viewed in color.

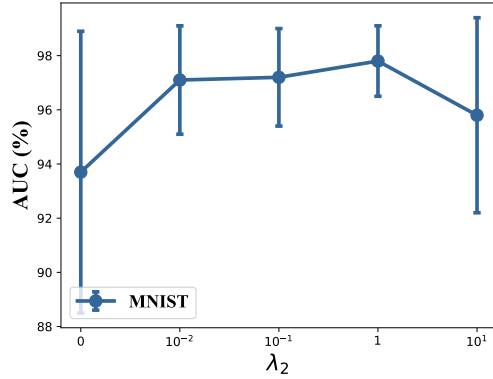


Figure 5. ESAD sensitivity analysis w.r.t. λ_1 on MNIST. We report avg. AUC with st. dev. over 90 experiments for various values of hyperparameter λ_2 . Best viewed in color.

ing of the autoencoder; (3) A novel model architecture is proposed to achieve effective end-to-end training; (4) Different from Deep SAD, both the two components which are related to the mutual information and the entropy are considered for the anomaly score measurement.

We further explain that these major changes are important. If we replace the $\mathcal{L}_{norm-semi}$ back to the SVDD loss, it is hard to achieve end-to-end training since the SVDD loss needs the initialization for the hypersphere center. In this case, the performance collapses to Deep SAD directly. If we replace $\mathcal{L}_{rec-semi}$ back to the original reconstruction loss in Deep SAD, the AUC on MNIST significantly reduces from 97.8% to 92.3% ($\gamma_l = 0.1, \gamma_p = 0.1$), while the original AUC for Deep SAD is 91.2%. This shows the importance of the optimization for the term related to the mutual information using the labeled outlier samples.